Numerical Study of Transient Thermal Ablation of High-Temperature Insulation Materials

Y. C. Shih*
National Taipei University of Technology, Taipei 106, Taiwan, Republic of China
F. B. Cheung†
Pennsylvania State University, University Park, Pennsylvania 16802
J. H. Koo‡
Texas A&M University, College Station, Texas 77843
and
B. C. Yang§
Industrial Technology Research Institute, Hsinchu 310, Taiwan, Republic of China

A physical model has been developed to describe the transient ablation phenomena of high-temperature insulation materials for the cases with and without the formation of a melt layer on the material surface. The model takes account of the effects of transient melt-layer formation, variable ablation temperatures, and heat of ablation of the material. Validity of the model has been demonstrated numerically by comparison with available analytical solutions for the special case of a constant ablation temperature. For the general case of variable ablation temperatures, appreciable differences in the predicted ablation rates have been found between the cases with and without melt-layer formation for materials having low heats of ablation and for large imposed external heat fluxes. The present study clearly indicates that the melt-layer effect cannot be neglected at high external heat fluxes, especially for materials such as MXBE-350 that have low heats of ablation.

Nomenclature

A	=	preexponential factor
A_P	=	cross-sectional area of grid element
a_E, a_P, a_W	=	discretized coefficient
b	=	source term
C	=	specific heat
E	=	activation energy
h	=	specific enthalpy
K	=	permeability
k	=	thermal conductivity
L	=	total length of the material
n	=	order of reaction
P	=	pressure
P	=	Peclet number
Q_a	=	heat of ablation
Q_d	=	heat of decomposition
q_e''	=	external heat flux
R	=	universal gas constant
S	=	net production within porous medium or ablation
$\dot{S}$	=	ablation rate
T	=	temperature
T_a	=	ablation temperature
t	=	time
u_b	=	velocity component in x direction
V	=	volume
V_p	=	volume of grid element
$\mathbf{v}_b$	=	velocity vector of moving solid
x	=	spatial coordinate
β	=	degree of char
Δt	=	time step
δx	=	length between grid nodes
ε	=	emissivity
Θ	=	temperature ($= T - T_0$)
μ	=	dynamic viscosity
ρ	=	density
Φ	=	porosity

Subscripts

c	=	char material
g	=	gas phase
m	=	melt layer
s	=	solid phase
v	=	virgin material
0	=	initial condition

Superscripts

0	=	previous time level
-	=	volume-averaging quantity or bulk value
^	=	intrinsic volume-averaging quantity or apparent value
*	=	dimensionless parameter

*Assistant Professor, Department of Air-Conditioning and Refrigerating Engineering.
†Professor, Department of Mechanical and Nuclear Engineering.
‡TEES Research Engineer, Department of Mechanical Engineering. Associate Fellow AIAA.
§Researcher, Energy and Resources Laboratories.

Introduction

HIGH-TEMPERATURE insulation materials have been employed extensively as thermal protection materials in a wide variety of military, aerospace, and structural applications. These materials often have been used as the liners of rocket propulsion systems and missile launching systems and the heat shields of atmospheric reentry vehicles to protect the substrates when exposed to hyperthermal environments. Most high-temperature insulation materials are carbon and silica fabric polymeric composites.[1] Among them,

the reinforced glass-filled polymeric composites, such as H41N and MXBE-350,[2] have been frequently utilized as the thermal barrier in military and aerospace applications because of their excellent high-temperature ablative performance. This type of material possesses the characteristics of high density, low porosity, high emissivity, high heat capacity, and low thermal conductivity, etc., which could sustain thermal attack in a high-temperature environment. The detailed mechanisms of heat transfer in high-temperature insulation materials have been described by Shih.[3] When the surrounding temperature or the imposed external heat flux is high enough, melting or recession or both of the material could occur on the surface. The surface ablation could become very severe when the material is subjected to the attack of a particle-laden flow.[4]

The ablation phenomena taking place at high temperatures have received considerable attention by a number of researchers in the past. Moyer and Rindal[5] developed a numerical model to predict the surface recession of high-temperature insulation materials, such as graphite or carbon-carbon composites. Blackwell and Hogan[6] proposed a numerical algorithm based upon Landau transformation and the finite control volume procedure to simulate one-dimensional problems with steady-state and transient ablation. Yang[7] and Yang et al.[8,9] developed a numerical model for predicting thermomechanical erosion of high-temperature insulation materials exposed to high-temperature, particle-laden flows such as the exhaust from a rocket engine. The materials used in such an environment are subjected not only to thermal attack but also to particle impact erosion. As a result, thermomechanical ablation of the material could take place.

In the preceding studies the eroded material produced by either thermal ablation or particle impact erosion was assumed to be effectively removed by the ambient gas stream. As such, no melt layer would form on the surface of the material. In reality, however, a melt layer could form on the surface of the material as observed in the experimental study of Chaboki et al.[10] The composition of the melt layer might include the deposit of the incoming particles and the eroded high-temperature insulation material. A number of studies[5,11–15] have been performed that considered the effect of melt-layer formation on the rate of heat penetration into the insulation material. However, they have been restricted to the case of quasi-steady material ablation with the formation of a steady melt layer on the material surface. It was found that the presence of a steady melt layer significantly reduces the rate of heat penetration and thus the overall erosion of the insulation material.

The authors of previous studies have focused primarily on the case of quasi-steady ablation with the presence of a steady melt layer on the eroded surface. Very little attention has been given to the case of transient ablation of the insulation material with the formation of a transient melt layer. In some applications the ablation phenomena could be highly transient, and therefore, it might not be valid to assume the process to be quasi-steady. Moreover, previous studies[11–15] have assumed that the ablation temperature is constant. In reality, however, the process is likely to occur over a range of temperatures. Thus, variable ablation temperatures should be considered in describing the ablation phenomena. The main objective of this study is to develop a physical model that is capable of predicting the transient thermal ablation phenomena, taking account of the effects of transient melt-layer formation, variable ablation temperatures, and heat of ablation of the material.

Development of an Ablation Model

The high-temperature insulation materials under consideration in the present study are glass-filled polymeric composites, such as H41N and MXBE-350.[2] For this type of materials, a layer of molten silica is likely to form on the eroded surface during the transient thermal ablation process, as observed by Chaboki et al.[10] When subjected to the thermal attack of a high-velocity, high-temperature flow, a residual char region would form on the surface. The residual char can then be removed by the flow, leaving the fiberglass exposed to the hyperthermal environment, which would subsequently be melted as the failure (melting) temperature of the insulation material is reached. The molten substance could cover the entire surface
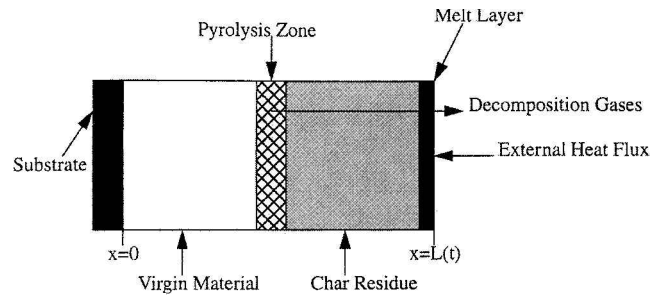

Fig. 1   Schematic of the four separate ablation regions.

as irregular liquid droplets or a thin liquid film. The thickness of the melt layer could reach several millimeters even though the material is subjected to the thermal attack of a high-speed flow.[16] In the case of aerodynamic ablation, the melt layer could be affected by the aerodynamic flow field. However, this is outside the scope of the present study.

In general, four separate regions including the virgin material, pyrolysis zone, char residue, and melt layer could develop in the materials, as shown in Fig. 1. Owing to the thermochemical expansion and surface ablation of the material, the interfaces separating these four regions are not stationary but moving with time. As such, the thermal response model developed by Shih[3] and Shih and Cheung[17] needs to be modified to account for these moving boundaries before the model can be applied to predict the thermal response of the material.

To formulate the problem, the conservative equations in an integral form for the space, mass, and energy quantities[18] are used to model the behavior of the high-temperature insulation material. In addition, the Eulerian–Lagrangian approach,[19,20] such as the Landau transformation, is adopted to make the moving boundaries stationary in the transformed coordinate before discretizing the governing equations. Two different cases are considered, one without and the other with the formation of a transient melt layer on the eroded surface.

Ablation Without a Melt Layer

This case corresponds to the special circumstances for which the molten substance is assumed to be instantaneously removed by the flow as soon as it is produced in the transient ablation process.

Governing Equations

The solid and the gas phases within the ablating material are treated separately with the gas flowing within the moving solid as a result of thermal expansion[3,17] and surface ablation of the material.

Solid phase.   The governing equations for the moving solid can be obtained by using the Leibniz rule[19]:

$$\frac{d}{dt}\left(\int_v f \, dV\right) = \int_v \frac{\partial f}{\partial t} \, dV + \int_A f \, \boldsymbol{v}_b \cdot \boldsymbol{n} \, dA \qquad (1)$$

where V and A are the volume and surface of the control volume, f the dependent quantity under consideration, $\boldsymbol{v}_b$ the velocity vector of the moving solid, and $\boldsymbol{n}$ the unit vector perpendicular to the surface.

Assuming the process of transient thermal ablation to be predominantly one-dimensional ($\boldsymbol{v}_b \cdot \boldsymbol{n} = u_b$), the governing equations of the moving solid for mass and energy quantities can be obtained by substituting $f = \bar{\rho}_s$ and $f = \bar{\rho}_s \hat{h}_s$ into Eq. (1), respectively. They are given as follows.

Conservation of mass:

$$\frac{d}{dt}\left(\int_V \bar{\rho}_s \, dV\right) = \int_V \frac{\partial \bar{\rho}_s}{\partial t} \, dV + \int_A \bar{\rho}_s u_b \, dA \qquad (2a)$$

The mass decomposition of the ablative material follows the Arrhenius equation,[3,17] so that Eq. (2a) can be expressed in the

following form by assigning $\partial \bar{\rho}_s / \partial t = \dot{\rho}_s$:

$$\frac{\mathrm{d}}{\mathrm{d}t}\left(\int_V \bar{\rho}_s \, \mathrm{d}V\right) - \int_A \bar{\rho}_s u_b \, \mathrm{d}A = \int_V \dot{\rho}_s \, \mathrm{d}V \qquad (2b)$$

$$\dot{\rho}_s = -\bar{\rho}_v A \left(\frac{\bar{\rho}_s - \bar{\rho}_v}{\bar{\rho}_v}\right)^n e^{-E/R\hat{T}_s} \qquad (2c)$$

From Eq. (2c) the density of solid material $\bar{\rho}_s$ can be solved explicitly. Moreover, the degree of char in an ablative material is defined as

$$\beta = \frac{\bar{\rho}_v - \bar{\rho}_s}{\bar{\rho}_v - \bar{\rho}_c} \qquad (2d)$$

Therefore, the weighted averages of the material properties, such as $\bar{k}_s$, Φ, and ε_s, can be estimated from β as follows:

$$\lambda = (1 - \beta)\lambda_v + \beta\lambda_c \qquad (2e)$$

Conservation of energy:

$$\frac{\mathrm{d}}{\mathrm{d}t}\left(\int_V \bar{\rho}_s \hat{h}_s \, \mathrm{d}V\right) = \int_V \frac{\partial}{\partial t}(\bar{\rho}_s \hat{h}_s)\, \mathrm{d}V + \int_A \bar{\rho}_s \hat{h}_s u_b \, \mathrm{d}A \qquad (3a)$$

By replacing the first term on the right-hand side of the preceding equation with the energy equation for the solid phase as derived in Refs. 3 and 17, Eq. (3a) can be written as follows:

$$\frac{\mathrm{d}}{\mathrm{d}t}\left(\int_V \bar{\rho}_s \hat{h}_s \, \mathrm{d}V\right) - \int_A \bar{\rho}_s \hat{h}_s u_b \, \mathrm{d}A = \int_A \bar{k}_s \frac{\partial \theta_s}{\partial x} \, \mathrm{d}A + \int_V S_s \, \mathrm{d}V \qquad (3b)$$

where S_s denotes the source or sink terms including the interfacial transfers between the solid and the gas phases and the energy consumption or generation during the pyrolysis reaction.[3,17]

Gas phase. The governing equations for the gas phase that flows within the moving solid must obey the conservation laws. The general conservative equation for the gas phase is given by Arpaci and Larsen,[18]

$$\frac{\mathrm{d}}{\mathrm{d}t}\left(\int_V f \, \mathrm{d}V\right) + \int_A f(\boldsymbol{v}_g - \boldsymbol{v}_b) \cdot \boldsymbol{n} \, \mathrm{d}A = -\int_A \boldsymbol{n} \cdot \boldsymbol{\varphi} \, \mathrm{d}A + \int_V S_\varphi \, \mathrm{d}V \qquad (4)$$

where f is the dependent quantity under consideration, $\boldsymbol{v}_g$ the velocity vector of the gas phase, and $\boldsymbol{\varphi}$ the flux of f and S_φ the source term. The continuity, energy, and pressure equations for the gas phase can be obtained from Eq. (4) as follows.

Continuity equation:
Setting $f = \bar{\rho}_g$ and $\varphi = 0$, we have

$$\frac{\mathrm{d}}{\mathrm{d}t}\left(\int_V \bar{\rho}_g \, \mathrm{d}V\right) + \int_A \bar{\rho}_g (\hat{u}_g - u_b) \, \mathrm{d}A = \int_V \dot{\rho}_g \, \mathrm{d}V \qquad (5)$$

where $\dot{\rho}_g = -\dot{\rho}_s$. The quantity $\dot{\rho}_s$ can be obtained from Eq. (2c).

Energy equation:
Substituting $f = \bar{\rho}_g \hat{h}_g$ and $-\boldsymbol{n} \cdot \boldsymbol{\varphi} = \bar{k}_g (\partial \theta_g / \partial x)$ into Eq. (4), it can be shown that

$$\frac{\mathrm{d}}{\mathrm{d}t}\left(\int_V \bar{\rho}_g \hat{h}_g \, \mathrm{d}V\right) + \int_A \bar{\rho}_g \hat{h}_g (\hat{u}_g - u_b) \, \mathrm{d}A$$

$$= \int_A \bar{k}_g \frac{\partial \theta_g}{\partial x} \, \mathrm{d}A + \int_V S_g \, \mathrm{d}V \qquad (6a)$$

where $S_g = -S_s$ and the gas-phase velocity $\hat{u}_g$ is determined by the Darcy–Forcheimer equation[3,17] as follows:

$$\hat{u}_g = -\frac{K}{\Phi\mu\gamma} \frac{\partial \hat{P}_g}{\partial x} \qquad (6b)$$

$$\gamma = 1 + C \cdot Re \qquad (6c)$$

$$Re = \frac{\sqrt{K}\hat{\rho}_g \Phi |\hat{u}_g|}{\mu} \qquad (6d)$$

Pressure equation:
By coupling the equation of state for an ideal gas with Eq. (5), the pressure equation can be written as

$$\frac{\mathrm{d}}{\mathrm{d}t}\left(\int_V \rho_d P^* \, \mathrm{d}V\right) - \int_A \rho_d P^* u_b \, \mathrm{d}A = \int_A \Gamma \frac{\partial P^*}{\partial x} \, \mathrm{d}A + \int_V \dot{\rho}_g \, \mathrm{d}V \qquad (7a)$$

$$\rho_d = \frac{\Phi \hat{P}_{g0}}{R\hat{T}_g} \qquad (7b)$$

$$P^* = \frac{\hat{P}_g}{\hat{P}_{g0}} \qquad (7c)$$

$$\Gamma = \hat{\rho}_g \frac{K}{\mu\gamma} P_{g0} \qquad (7d)$$

Landau Transformation

Landau transformation has been used in the past in Refs. 6, 19, and 20 to immobilize the moving boundary in modeling thermal ablation and phase change problems. The Landau transformation is based on the use of a moving coordinate defined by

$$\xi = x/L(t) \qquad (8)$$

where $L(t)$ is the time-dependent instantaneous length of the material, as shown in Fig. 1. The quantity $L(t)$ is a major unknown, which would vary with time as a result of thermochemical expansion[3,17] and material ablation. In the transformed moving coordinate the domain of interest is fixed between $\xi = 0$ and 1. The movement of the solid phase in the transformed domain must obey the space conservation law[6]

$$\frac{\mathrm{d}}{\mathrm{d}t}\int_V \mathrm{d}V = \int_A u_b \, \mathrm{d}A \qquad (9a)$$

which can be expressed by

$$u_b = \frac{\mathrm{d}L}{\mathrm{d}t}\xi \qquad (9b)$$

Discretized Equations

Applying Landau transformation and the finite volume method[21] to the governing equations for the solid and the gas phases, the following discretized equations can be obtained.

Energy equation for the solid phase:

$$a_P(\theta_s)_P = a_E(\theta_s)_E + a_W(\theta_s)_W + b \qquad (10)$$

where

$$a_P = (\bar{\rho}_s \bar{C}_m)_P^0 \frac{L^0 \Delta \xi_P A_P}{\Delta t} + a_E + a_W \qquad (11a)$$

$$a_E = D_e A(|P_e|) + [-F_e, 0] \qquad (11b)$$

$$a_W = D_w A(|P_w|) + [F_w, 0] \qquad (11c)$$

$$\bar{C}_m = \frac{(1 - \beta)\bar{\rho}_v \bar{C}_v + \beta \bar{\rho}_c \bar{C}_c}{\bar{\rho}_s} \qquad (11d)$$

$$D = \bar{k}_s \frac{A_P}{\delta x} \quad (11e)$$

$$F = \bar{\rho}_s \bar{C}_m (-u_b) A_P \quad (11f)$$

$$A(|P|) = [0, (1 - |P|)^5] \quad (11g)$$

$$P = \frac{F}{D} \quad (11h)$$

$$b = \left[\frac{(\bar{\rho}_s \bar{C}_m)_P^0 (\theta_s)_P^0}{\Delta t} + (S_s)_P - (\dot{\rho}_s \bar{C}_m \theta_s)_P \right] L^0 \Delta \xi_P A_P \quad (11i)$$

In the preceding discretized equations the method of mixture enthalpy[3,17] has been used to formulate the enthalpy term for the solid phase.

Energy equation for the gas phase:

$$a_P (\theta_g)_P = a_E (\theta_g)_E + a_W (\theta_g)_W + b \quad (12)$$

where

$$a_P = (\bar{\rho}_g \bar{C}_g)_P^0 \frac{L^0 \Delta \xi_P A_P}{\Delta t} + a_E + a_W \quad (13a)$$

$$a_E = D_e A(|P_e|) + [-F_e, 0] \quad (13b)$$

$$a_W = D_w A(|P_w|) + [F_w, 0] \quad (13c)$$

$$\bar{C}_g = \frac{\int_{\hat{T}_0}^{\hat{T}_g} C_g \, dT}{\hat{T}_g - \hat{T}_0} \quad (13d)$$

$$D = \bar{k}_g \frac{A_P}{\delta x} \quad (13e)$$

$$F = \bar{\rho}_g \bar{C}_g (\hat{u}_g - u_b) A_P \quad (13f)$$

$$A(|P|) = [0, (1 - |P|)^5] \quad (13g)$$

$$P = \frac{F}{D} \quad (13h)$$

$$b = \left[\frac{(\bar{\rho}_g \bar{C}_g)_P^0 (\theta_g)_P^0}{\Delta t} + (S_g)_P - (\dot{\rho}_g \bar{C}_g \theta_g)_P \right] L^0 \Delta \xi_P A_P \quad (13i)$$

Pressure equation:

$$a_P P_P^* = a_E P_E^* + a_W P_W^* + b \quad (14)$$

where

$$a_P = \frac{(\rho_d)_P}{\Delta t} L \Delta \xi_P A_P + D_e + D_w + ([F_e, 0] + [-F_w, 0]) \quad (15a)$$

$$a_E = [-F_e, 0] + D_e \quad (15b)$$

$$a_W = [F_w, 0] + D_w \quad (15c)$$

$$F = -\rho_d u_b A_P \quad (15d)$$

$$D = \frac{\Gamma}{\delta x} A_P \quad (15e)$$

The upwind scheme is used to deal with the convection term in the preceding equations.

Surface Ablation

With the eroded surface being exposed to an external heat flux q_e'', an energy balance on the material surface leads to

$$q_e'' - \bar{k}_s \frac{\partial \hat{T}_s}{\partial x} \bigg|_{x=L} = \bar{\rho}_s Q_a \frac{dS}{dt} \quad (16a)$$
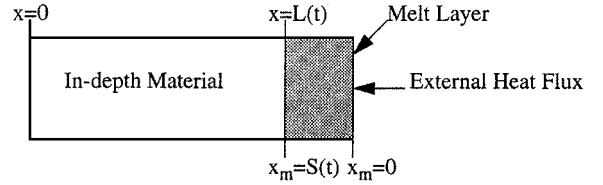

Fig. 2   Domain of interest for the in-depth material and the melt layer.

where dS/dt is the rate of ablation.

In Eq. (16a) heat of ablation Q_a is defined as[17]

$$Q_a = q_0''/\dot{m} \quad (16b)$$

where q_0'' is the external heat flux to a nonablating wall at the ablating temperature and $\dot{m}$ the mass ablation rate of the material.

Ablation with a Melt Layer

For the general case of ablation with the formation of a transient melt layer, the solution domain needs to be divided into two parts: in-depth material and melt layer. The origin of the in-depth material is fixed on the substrate side, whereas that of the melt layer is set at the melt surface exposed to the external heat flux, as depicted in Fig. 2. The governing equations for the in-depth material including the solid and the gas phases are essentially the same as those just given. For the melt layer the governing equations are obtained by assuming that the thermophysical properties of the melt layer are constant. For a thin melt layer this is considered a good approximation.

Governing Equations for the Melt Layer

Following the Leibniz rule the energy equation can be written as

$$\frac{d}{dt} \left(\int_v \rho_m C_m \theta_m \, dV \right) - \int_A \rho_m C_m \theta_m \frac{dS}{dt} \, dA = \int_A k_m \frac{\partial \theta_m}{\partial x} \, dA \quad (17)$$

where subscript m refers to the melt layer and $\theta_m = T_m - T_0$.

Discretized Equation

By applying the Landau transformation $\xi = x/S(t)$ and the finite volume method, Eq. (17) can be discretized as

$$a_P (\theta_m)_P = a_E (\theta_m)_E + a_W (\theta_m)_W + b \quad (18)$$

where

$$a_P = (\rho_m C_m)_P^0 \frac{S^0 \Delta \xi_P A_P}{\Delta t} + a_E + a_W \quad (19a)$$

$$a_E = D_e A(|P_e|) + [-F_e, 0] \quad (19b)$$

$$a_W = D_w A(|P_w|) + [F_w, 0] \quad (19c)$$

$$b = \frac{(\rho_m C_m)_P^0 (\theta_m)_P^0}{\Delta t} S^0 \Delta \xi_P A_P \quad (19d)$$

in which D, F, and $A(|P|)$ are defined the same as before.

Interface Condition

An energy balance at the interface $L(t)$ or $S(t)$ between the in-depth material and the melt layer gives

$$k_m \frac{\partial \theta_m}{\partial x} \bigg|_m - \bar{k}_s \frac{\partial \theta_s}{\partial x} \bigg|_s = \rho_m Q_a \frac{dS}{dt} \quad (20)$$

Numerical Algorithm

A numerical iterative algorithm has been developed to calculate the temperature distribution of the material and the rate of ablation. Because the process of ablation usually occurs over a temperature range, the numerical algorithm is written to account for variable

ablation temperatures. For the special case without the formation of a melt layer, the temperature profile in the in-depth material is solved from Eqs. (10–15) by assuming a value for the rate of ablation. The ablation rate is then updated from Eq. (16a) using the calculated temperature field for the in-depth material. The preceding procedure is repeated until all of the solutions are converged.

For the case with the formation of a melt layer, the governing equations for the in-depth material and the melt layer are solved separately, and the interface condition given by Eq. (20) is used to connect both fields. The initial thickness of the melt layer is assumed to be sufficiently small so that the solution of the initiating ablation for the case without a melt layer can be used to provide the initial conditions for the in-depth material. The temperatures for the in-depth material and the melt layer are calculated respectively from Eqs. (10–15) and Eqs. (18) and (19) by assuming a value for the rate of ablation. The ablation rate is then updated from Eq. (20) using the new temperature fields just calculated for the in-depth material and the melt layer. The preceding procedure is repeated until all of the solutions are converged.

Results and Discussion

To verify the accuracy of the numerical iteration scheme, the model is applied to predict the ablation of a solid exposed to an imposed external heat flux, assuming that no melt layer is present on the material surface and that the process takes place at a constant ablation temperature. For this special case analytical solutions have been obtained in Refs. 5 and 6. The thermophysical properties employed in the numerical calculations are $\rho = 1600 \, \text{kg/m}^3$, $C = 2000 \, \text{J/kg-K}$, $k = 2 \, \text{W/m-K}$, $T_0 = 400 \, \text{K}$, $T_a = 1400 \, \text{K}$, and $Q_a = 2 \times 10^6 \, \text{J/kg}$. The imposed external heat flux q_e'' is set equal to $2 \times 10^3 \, \text{kW/m}^2$, and the substrate temperature at $x = 0$ is set at $T = 400 \, \text{K}$. In this case the total length of the material is chosen to be 10 cm in order to simulate the ablation under quasi-steady conditions. A comparison of the present numerical results and the exact solution is depicted in Fig. 3, and the agreement is found to be highly satisfactory. Moreover, as shown in Table 1, the relative errors in the ablation rates between the numerical and analytical solutions are found to de-

crease as the mesh size and time step are refined in the numerical calculations. This demonstrates the grid independence of the present results.

To verify the accuracy of the present numerical iteration scheme further, the model is also applied to predict the ablation rate of a semi-infinite solid material that has a constant melting or ablation temperature, which is equal to 1400 K. The temperature at $x = 0$ is kept at 400 K. The surface temperature is assumed to be 1500 K, and a transient melt layer is considered to grow on the eroded surface once the melting temperature of the material is reached. A solid material with the length of 2.5 m is used to simulate a semi-infinite solid. The thermophysical properties of the solid material and the melt layer are assumed to be the same, having the same values as those employed in Fig. 3. In this case the initial thickness of the melt layer is assumed to be 0.01% of total material length. The interface position between the solid and liquid phases (i.e., between the solid material and the growing melt layer) predicted by the present model is compared with the exact solution[22] in Fig. 4, and the agreement is found to be highly satisfactory. The relative errors in the predicted interface position are found to decrease as the mesh size and time step are refined in the numerical calculations, as displayed in Table 2. This further demonstrates the grid independence of the present results.

Having verified the accuracy of the numerical iteration scheme, the present model is employed to perform numerical calculations for the general case of variable ablation temperatures for two different high-temperature insulation materials, that is, H41N and MXBE-350. The thermophysical properties of H41N and MXBE-350 are given in Tables 3 and 4.[3,17] In addition, decomposition gas properties are listed in Table 5.[3,17] Figure 5 shows the predicted ablation for H41N assuming no melt-layer formation. The failure temperature of H41N is set at 1800 K, and thermal ablation of the material is considered to initiate once this failure temperature is reached. In addition, the heat of ablation of $1.442 \times 10^7 \, \text{J/kg}$ measured by Koo et al.[23] is employed in the calculations. The H41N material with the initial length of 1.27 cm is exposed to an imposed external heat flux of $q_e'' = 7.38 \times 10^3 \, \text{kW/m}^2$ for 5.2 s. At the end of this period, the

Table 1   Relative errors in the predicted ablation rates for the refinement of mesh size and time step at $t = 16$ s (Exact solution: ablation rate $\dot{S} = 3.125 \times 10^{-4}$ m/s)

No. of mesh	Δx, m	Δt, s	$\dot{S}$ @ 16 s, m/s	Relative error, %
50	0.002	0.64	3.466×10^{-4}	10.91
100	0.001	0.16	3.224×10^{-4}	3.17
200	0.0005	0.04	3.153×10^{-4}	0.90

Table 2   Relative errors in the predicted interface positions for the refinement of mesh size and time step at $t = 10^5$ s (Exact solution: interface position $S = 0.036$ m)

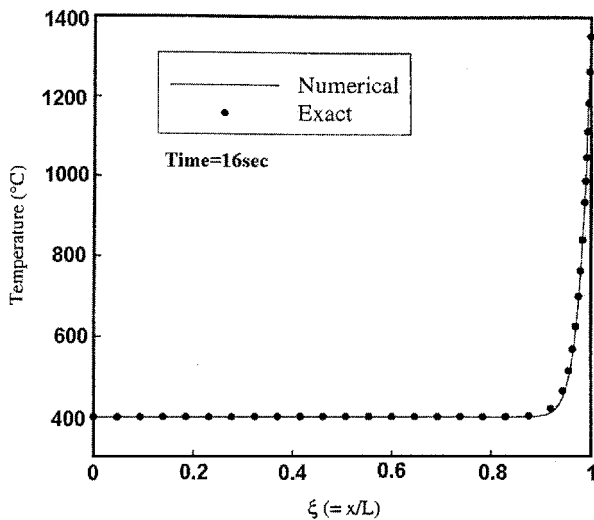| No. of mesh	Δx, m	Δt, s	S, m	Relative error, %
100	0.025	2	0.036195	0.542
200	0.0125	0.5	0.036185	0.514
400	0.00625	0.125	0.036176	0.489

Fig. 3   Comparison of the calculated temperature distribution with the exact solution for the case of a constant ablation temperature (no melt layer).
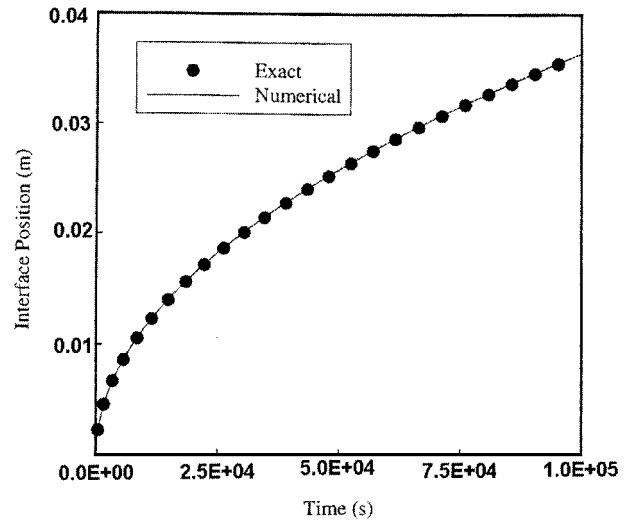

Fig. 4   Comparison of the calculated interface position with the exact solution for the case of a constant ablation temperature (with a melt layer).

Table 3   Material properties for H41N

Property/parameter	Function[a]	Range[a]
ρ_v, kg/m³	1810.0	——
ρ_c, kg/m³	1440.0	——
k_v, W/m/K	$0.80 + 2.76 \times 10^{-4}\ T$	$20 \leq T \leq 1000$
k_c, W/m/K	$0.96 + 8.42 \times 10^{-4}\ T$ $-4.07 \times 10^{-6}\ T^2$ $+ 5.32 \times 10^{-9}\ T^3$	$20 \leq T \leq 1000$
C_v, kJ/kg/K	$1.05 + 9.76 \times 10^{-4}\ T$	$20 \leq T \leq 1200$
C_c, kJ/kg/K	$0.88 + 7.60 \times 10^{-4}\ T$	$20 \leq T \leq 1200$
Φ_v	0.113	——
Φ_c	0.274	——
K_v, m²	6.18×10^{-18}	——
K_c, m²	4.85×10^{-15}	——
A, 1/s	1.98×10^{29}	$m_s/m_0 \geq 0.91$
	8.17×10^{18}	$0.795 \leq m_s/m_0 < 0.91$
	2.62×10^{7}	$m_s/m_0 < 0.795$
E, kJ/kmol	2.60×10^{5}	$m_s/m_0 \geq 0.795$
	3.54×10^{5}	$m_s/m_0 < 0.795$
n (−)	17.33	$m_s/m_0 \geq 0.91$
	6.30	$0.795 \leq m_s/m_0 < 0.91$
	0.53	$m_s/m_0 < 0.795$
Q_d, kJ/kg	−234.0	$m_s/m_0 \geq 0.795$
	−2093.0	$m_s/m_0 < 0.795$
Q_a, kJ/kg	1.442×10^{4}	——
ε_v	0.84	——
ε_c	0.88	——

[a]Temperature in degrees Celsius.

Table 4   Material properties for MXBE-350

Property/parameter	Function[a]	Range[a]
ρ_v, kg/m³	1720.0	——
ρ_c, kg/m³	1204.0	——
k_v, W/m/K	$0.64 + 1.14 \times 10^{-5}\ T$	$20 \leq T \leq 1000$
k_c, W/m/K	$0.50 + 1.88 \times 10^{-3}\ T$ $-6.36 \times 10^{-6}\ T^2 +$ $6.74 \times 10^{-9}\ T^3$	$20 \leq T \leq 1000$
C_v, kJ/kg/K	$1.26 + 4.61 \times 10^{-4}\ T$	$20 \leq T \leq 800$
C_c, kJ/kg/K	$0.67 + 7.12 \times 10^{-4}\ T$	$20 \leq T \leq 800$
Φ_v	0.124	——
Φ_c	0.340	——
K_v, m²	2.73×10^{-17}	——
K_c, m²	1.82×10^{-13}	——
A, 1/s	2.48×10^{44}	$m_s/m_0 \geq 0.96$
	8.47×10^{16}	$0.70 \leq m_s/m_0 < 0.96$
	8.65×10^{6}	$m_s/m_0 < 0.70$
E, kJ/kmol	2.20×10^{5}	$m_s/m_0 \geq 0.70$
	3.42×10^{5}	$m_s/m_0 < 0.70$
n (−)	50.64	$m_s/m_0 \geq 0.96$
	4.20	$0.70 \leq m_s/m_0 < 0.96$
	0.21	$m_s/m_0 < 0.70$
Q_d, kJ/kg	−553.0	$m_s/m_0 \geq 0.70$
	−2093.0	$m_s/m_0 < 0.70$
Q_a, kJ/kg	4.724×10^{3}	——
ε_v	0.80	——
ε_c	0.80	——

[a]Temperature in degrees Celsius.

Table 5   Decomposition gas properties

Property/parameter	Function[a]	Range[a]
k_g, W/m/K	$0.03 + 1.40 \times 10^{-4}\ T$	$20 \leq T \leq 1000$
C_g, kJ/kg/K	$2.39 + 1.05 \times 10^{-3}\ T$	$20 \leq T \leq 800$
μ_g, kg/m/s	$1.48 \times 10^{-5} + 2.50 \times 10^{-8}\ T$	$20 \leq T \leq 800$
M, kg/kmol	18.35	——
C	73.61	——

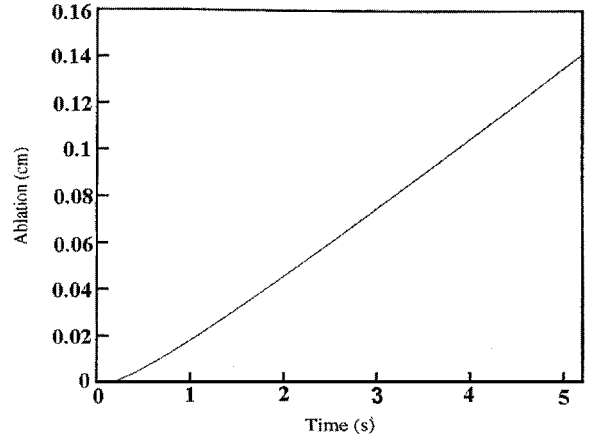[a]Temperature in degrees Celsius.

Fig. 5   Predicted extent of ablation for H41N for the case without a melt layer.
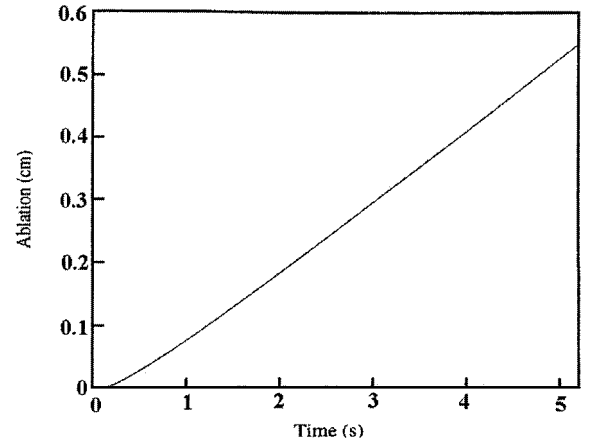

Fig. 6   Predicted extent of ablation for MXBE-350 for the case without a melt layer.

possible explanation for this relatively large discrepancy could be because of the uncertainty in the failure temperature of MXBE-350.

From the experimental data[23] it is known that H41N and MXBE-350 have appreciably different heats of ablation. The heat of ablation of H41N is nearly three times larger than that of MXBE-350. Thus, when subjected to the same imposed heat flux, the ablation rates for both materials could be quite different. Figures 7–10 show, respectively, the predicted amounts of ablation for H41N and MXBE-350 and the calculated rates of ablation for the two materials. In these figures the initial length of the material is 3 cm, and the imposed external heat flux is $q_e'' = 2 \times 10^3$ kW/m². For the purpose of comparison, the predicted amounts of ablation for the cases with and without melt-layer formation are also shown in these figures. To predict the thermal response of melt layer, the properties of melt layer used in this study are shown in Table 6. MXBE-350 has a higher ablation rate than H41N mainly because it has a smaller heat of ablation. The differences in the amounts and the rates of ablation for the cases with and without a melt layer are considerably larger for MXBE-350 than H41N. This result reveals that the smaller the heat of ablation, then the larger the effect of the melt layer.

calculated ablation is about 0.141 cm as compared to the measured value of 0.147 cm by Koo et al.[23] The relative error is only 4%, which clearly demonstrates the accuracy of the present model.

Figure 6 shows the predicted ablation for MXBE-350 assuming no melt-layer formation. Owing to the uncertainty of the failure temperature for MXBE-350, the same failure temperature for H41N (i.e., 1800 K) is employed in calculating the ablation of MXBE-350. The heat of ablation is set at 4.724×10^6 J/kg, as measured by Koo et al.[23] The MXBE-350 material with the initial length of 1.27 cm is exposed to an imposed external heat flux of $q_e'' = 7.38 \times 10^3$ kW/m² for 5.2 second. At the end of this period, the calculated ablation is about 0.550 cm, as compared to the measured value of 0.472 cm by Koo et al.[23] The relative error is almost 16.5% in this case. A

Table 6   Melt-layer properties of H41N and MXBE-350

Property/parameter	H41N	MXBE-350
ρ_m, kg/m³	1440.0	1204.0
k_m, W/m/K	3.052	2.76
C_m, kJ/kg/K	1.792	1.24

**Table 7a   Effect of external heat flux on ablation of H41N: $q_e'' = 2 \times 10^6$ W/m², t@52 s**

With/without melt layer	Ablation, cm	Ablation rate, cm/s	Q_0, W/m²	Q_i, W/m²	$(q_e'' - Q_0)/q_e$
With	0.301	0.00624	1.77×10^6	4.15×10^5	11.5%
Without	0.327	0.00746	2×10^6	4.28×10^5	0%

Table 7b   Effect of external heat flux on ablation of H41N: $q_e'' = 4 \times 10^6$ W/m², t@25 s

With/without melt layer	Ablation, cm	Ablation rate, cm/s	Q_0, W/m²	Q_i, W/m²	$(q_e'' - Q_0)/q_e$
With	0.302	0.00121	3.19×10^6	6.43×10^5	20.2%
Without	0.351	0.00157	4×10^6	6.97×10^5	0%

Table 7c   Effect of external heat flux on ablation of H41N: $q_e'' = 8 \times 10^6$ W/m², t@12.7 s

With/without melt layer	Ablation, cm	Ablation rate, cm/s	Q_0, W/m²	Q_i, W/m²	$(q_e'' - Q_0)/q_e$
With	0.298	0.00213	5.5×10^6	1.01×10^5	31.2%
Without	0.383	0.00324	8×10^6	1.18×10^5	0%
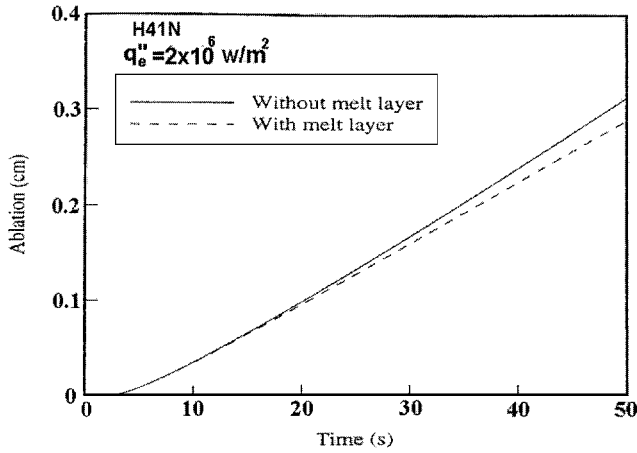
Fig. 7   Predicted extent of ablation for H41N for the cases with and without a melt layer.
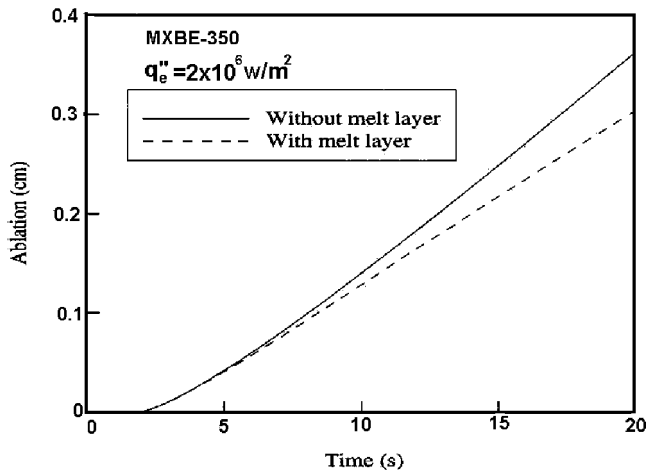
Fig. 8   Predicted extent of ablation for MXBE-350 for the cases with and without a melt layer.
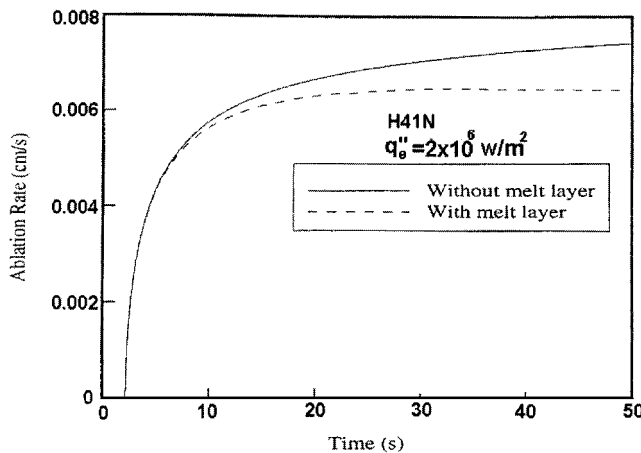
Fig. 9   Predicted ablation rate for H41N for the cases with and without a melt layer.
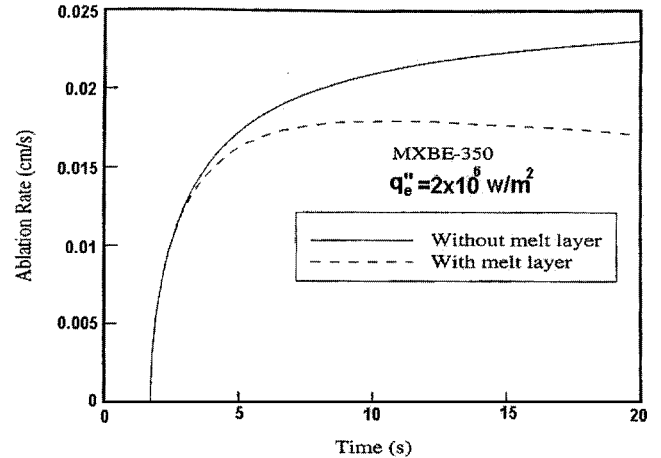
Fig. 10   Predicted ablation rate for MXBE-350 for the cases with and without a melt layer.

Figures 11 and 12 present an energy balance on the material surface for the cases with and without a melt layer for H41N and MXBE 350, respectively. In these figures Q_0 is equal to the first term on the left-hand side of Eqs. (16) and (20), Q_i the second term on the left-hand side, and Q_{net} the term on the right-hand side. For both H41N and MXBE-350 the difference in the value of Q_i for the cases with and without a melt layer is relatively small, whereas the difference in the value of Q_0 is considerably larger, especially for MXBE-350. The melt layer tends to grow faster for MXBE-350, and as such, a larger amount of energy tends to trap within the melt layer as compared with that of H41N. Therefore, for MXBE-350 there is larger difference in the value of Q_{net} between the cases with and without a melt layer.

Tables 7a–7c show the effect of the imposed external heat flux on the amounts and the rates of ablation. The material being considered is H41N having the initial length of 3 cm. Three different imposed external heat fluxes, equal to 2×10^3 kW/m², 4×10^3 kW/m², and 8×10^3 kW/m², respectively, are explored in this study. As can be seen from the table, the larger the external heat flux is, the greater the differences in the extent and the rate of ablation between the cases with and without a melt layer.

Figure 13 shows the relation between Q_0 and the thickness of the melt layer for MXBE-350. In this figure the experimental conditions employed by Chaboki et al.[10] are adopted in this study. The
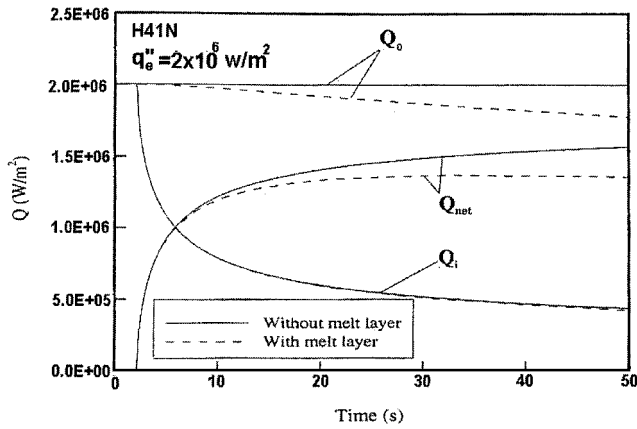
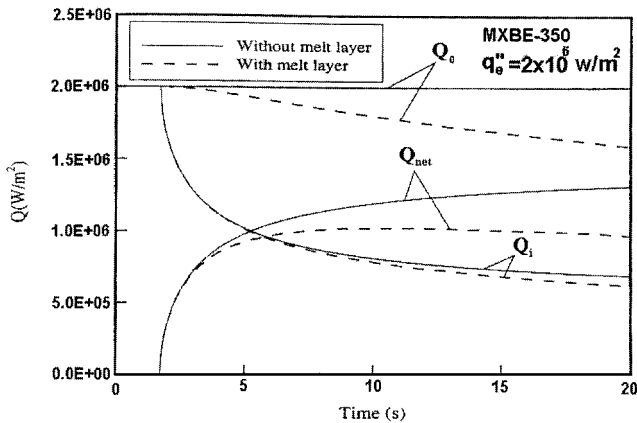**Fig. 11   Energy balance on the H41N surface for the cases with and without a melt layer.**

Fig. 12   Energy balance on the MXBE-350 surface for the cases with and without a melt layer.
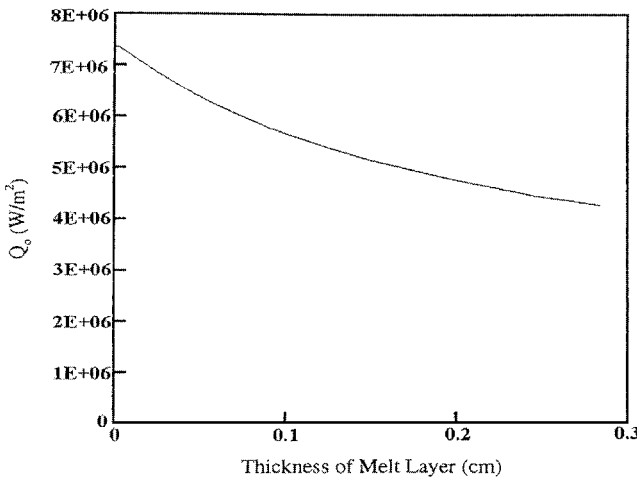

Fig. 13   Relation between Q_0 and the melt-layer thickness for MXBE-350.

high-temperature material, that is, MXBE-350, having the initial length of 1.27 cm, is exposed to a high-temperature torch that gives rise to an imposed heat flux of 7.38×10^3 kW/m^2. Even though the thickness of the melt layer is as small as 0.5 mm, the melt layer can absorb 15% of the imposed heat flux. This clearly indicates that the presence of a melt layer could appreciably reduce the rate of heat transfer to the interior side of the insulation material. This is true especially for materials with a low heat of ablation, such as MXBE-350. Additional experimental data from Koo et al.[24,25] were recently available to the authors to further validate this model in our next study.

Conclusion

A physical model has been developed to describe the transient phenomena of thermal ablation of high-temperature insulation materials for the cases with and without the formation of a melt layer on the eroded surface. The model has been applied to H41N that has a larger heat of ablation and to MXBE-350 that has a smaller heat of ablation. When exposed to the same external heat flux, the growth rate of the melt layer for MXBE-350 is found to be considerably higher than that of H41N. Also, much larger differences in the ablation rates for the cases with and without a melt layer are observed for MXBE-350 when compared to H41N. For a given insulation material the difference in the predicted ablation rates between the cases with and without a melt layer becomes appreciably larger as the imposed external heat flux is increased. When a high-temperature insulation material with a low heat of ablation is exposed to a high external heat flux, the melt layer tends to grow quickly, and as such, a large portion of energy is likely to be trapped within the melt layer under such a circumstance. The protective effect of the melt layer cannot be neglected at high external heat fluxes for materials such as MXBE-350, which have small heats of ablation. Additional experimental data are needed to further validate our model.

References

[1] Schmidt, D. L., "Ablative Polymers in Aerospace Technology," *Ablative Plastics*, edited by G. F. D'Alelio, and J. A. Parker, Marcel Dekker, New York, 1971, pp. 1–39.

[2] Tant, M. R., and Henderson, J. B., "Thermochemical Expansion of Polymer Composites," *Handbook of Ceramics and Composites*, Vol. 1, edited by N. P. Cheremisinoff, Marcel Dekker, New York, 1990, pp. 387–412.

[3] Shih, Y. C., "Thermochemical Ablation of High-Temperature Thermal Insulation Materials," Ph.D. Dissertation, Dept. of Mechanical Engineering, Pennsylvania State Univ., University Park, PA, Dec. 1997.

[4] Ungar, E. W., "Particle Impacts on the Melt Layer of an Ablating Body," *ARS Journal*, Vol. 30, No. 9, 1960, pp. 799–805.

[5] Moyer, C. B., and Rindal, R., "An Analysis of the Coupled Chemically Reacting Boundary Layer and Charring Ablator," NASA CR 1061, June 1968.

[6] Blackwell, B. F., and Hogan, R. E., "One-Dimensional Ablation Model Using Landau Transformation and Finite Control Volume Procedure," *Journal of Thermophysics and Heat Transfer*, Vol. 8, No. 2, 1994, pp. 282–287.

[7] Yang, B. C., "A Theoretical Study of Thermo-Mechanical Erosion of High-Temperature Ablatives," Ph.D. Dissertation, Dept. of Mechanical Engineering, Pennsylvania State Univ., University Park, PA, Dec. 1992.

[8] Yang, B. C., Cheung, F. B., and Koo, J. H., "Modeling of One-Dimensional Thermomechanical Erosion of the High-Temperature Ablatives," *Journal of Applied Mechanics*, Vol. 60, Dec. 1993a, pp. 1027–1032.

[9] Yang, B. C., Cheung, F. B., and Koo, J. H., "Numerical Investigation of Thermo-Chemical and Mechanical Erosion of Ablative Materials," AIAA Paper 93-2045, June–July 1993.

[10] Chaboki, A., Kneer, M. J., Schneider, M. E., and Koo, J. H., "Supersonic Torch Facility for Ablative Testing," AIAA Paper 90-1761, June 1990.

[11] Bethe, H. A., and Adams, M. C., "A Theory for the Ablation of Glassy Materials," *Journal of the Aero/Space Sciences*, Vol. 26, No. 6, 1959, pp. 321–328.

[12] Lees, L., "Similarity Parameters for Surface Melting of a Blunt Nosed Body in a High Velocity Gas Stream," *ARS Journal*, May 1959, pp. 345–354.

[13] Hsieh, C.-L., and Seader, J. D., "Surface Ablation of Silica-Reinforced Composites," *AIAA Journal*, Vol. 11, No. 8, 1973, pp. 1181–1187.

[14] Hsieh, C.-L., and Seader, J. D., "Similarity Analysis for the Surface Ablation of Silica-Reinforced Composites," *Journal of Spacecraft and Rockets*, Vol. 10, No. 12, 1973, pp. 797–802.

[15] Cheung, F. B., Yang, B. C., Burch, R. L., and Koo, J. H., "Effect of Melt Layer on Thermo-Mechanical Erosion of High-Temperature Ablative Materials," *Proceedings of the Pacific International Conference on Aerospace Science and Technology*, Vol. 1, National Cheng Kung Univ., Taiwan, 1993, pp. 41–48.

[16] Steverding, B., "A Theory for the Ablation of Non-Newtonian Liquids near the Stagnation Point," *AIAA Journal*, Vol. 3, No. 7, 1965, pp. 1245–1249.

[17] Shih, Y. C., and Cheung, F. B., "A Numerical Study of the Thermal Response of High-Temperature Ablative Materials," *Numerical Heat Transfer, Part A: Applications*, Vol. 32, No. 5, 1997, pp. 555–574.

[18] Arpaci, V. S., and Larsen, P. S., *Convection Heat Transfer*, Prentice-Hall, Upper Saddle River, NJ, 1984, pp. 24–34.

[19] Hsu, C. F., Sparrow, E. M., and Patankar, S. V., "Numerical Solution of Moving Boundary Problems by Boundary Immobilization and a Control-Volume-Based Finite-Difference Scheme," *International Journal of Heat and Mass Transfer*, Vol. 24, No. 8, 1981, pp. 1335–1343.

[20] Lacroix, M., and Garon, A., "Numerical Solution of Phase Change Problems: an Eulerian-Lagrangian Approach," *Numerical Heat Transfer*, Vol. 19B, No. 1, 1992, pp. 57–78.

[21] Patankar, S. V., *Numerical Heat Transfer and Fluid Flow*, Hemisphere, Washington, DC, 1980, pp. 41–102.

[22] Özisik, M. N., *Heat Conduction*, Wiley, New York, 1980, pp. 397–412.

[23] Koo, J. H., Lin, S., Kneer, M., and Miller, M., "Comparison of Ablative Materials in a Simulated Solid Rocket Exhaust Environment," AIAA Paper 91-0978, April 1991.

[24] Koo, J. H., Stretz, H., Bray, A., Wootan, W., Mulich, S., Powell, B., Weispfenning, J., and Grupa, T., "Phenolic-Clay Nanocomposites for Rocket Propulsion System," *Proceedings of the SAMPE 2002 International Symposium*, Vol. 47, Society for the Advancement of Materials and Process Engineering, Covina, CA, 2002, pp. 1085–1098.

[25] Koo, J. H., Stretz, H., and Bray, A. V., "Next Generation Nanostructured Ablatives for Rocket Propulsion," Air Force Office of Scientific Research, STTR Phase I Final Rept., Arlington, VA, Sept. 2001.